Fuel 379 (2025) 133115

Contents lists available at ScienceDirect

Fuel

journal homepage: www.elsevier.com/locate/fuel

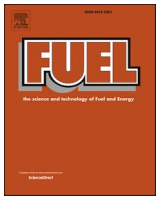

Full Length Article

Effect of macro-structure of Ni-based catalysts on methane splitting systems

Luís Alves [a,b], Vítor Pereira [a,b], Paula Dias [a,b], Tiago Lagarteira [a,b], Simone Meloni [c], Gonzalo Prieto [d], Adélio Mendes [a,b,*]

[a] LEPABE - Laboratory for Process Engineering, Environmental, Biotechnology and Energy, Faculty of Engineering, University of Porto, Rua Dr. Roberto Frias, 4200-465 Porto, Portugal
[b] ALiCE – Associated Laboratory in Chemical Engineering, Faculty of Engineering, University of Porto, Rua Dr. Roberto Frias, 4200-465 Porto, Portugal
[c] Department of Chemical, Pharmaceutical and Agricultural Sciences, University of Ferrara, Via Luigi Borsari 46, 44121 Ferrara, Italy
[d] ITQ - Instituto de Tecnología Química, Universitat Politècnica de València-Consejo Superior de Investigaciones Científicas (UPV-CSIC), Av. Los Naranjos, s/n, 46022 Valencia, Spain

ARTICLE INFO

Keywords:
Methane splitting
Methane decomposition
Hydrogen
Catalytic films
CO_x-free
Carbon

ABSTRACT

Methane splitting, also known as methane decomposition or cracking, is an emergent technology to allow swift energy decarbonization since it produces hydrogen without emitting CO_2. This work aims at improving hydrogen production from low temperature methane splitting process catalyzed on Ni surfaces. Six different systems were evaluated for their productivity: Ni-foil (pristine and acid treated), Ni particles deposited on α–Al_2O_3 and on carbon felt, and SiO_2-Al_2O_3-supported Ni catalyst deposited on α–Al_2O_3 and on carbon felt. Ni-foil displayed negligible hydrogen production even after chemical abrasion treatments were used to increase the surface area. For α–Al_2O_3 substrates, the coating of Ni/SiO_2-Al_2O_3 vastly outperformed the bulk Ni system (*ca.* 40 *vs* 0.011 $g_{H2}{\cdot}g_{Ni}^{-1}$ total hydrogen production). Depositing bulk Ni on carbon felt improved total hydrogen production to *ca.* 0.095 $g_{H2}{\cdot}g_{Ni}^{-1}$. Ni/SiO_2-Al_2O_3 deposited over carbon felt was particularly stable (40 $g_{H2}{\cdot}g_{Ni}^{-1}$ total hydrogen production), presenting an activity loss rate of *ca.* 0.011$\cdot g_{H2}{\cdot}g_{Ni}^{-1}{\cdot}h^{-2}$, compared to *ca.* 0.020 $g_{H2}{\cdot}g_{Ni}^{-1}{\cdot}h^{-2}$ for the Ni/SiO_2-Al_2O_3 deposited over α–Al_2O_3. Furthermore, the mechanical integrity of the carbon felt-deposited film was shown to be maintained, while the α–Al_2O_3-deposited film structure collapsed, due to carbon formation.

1. Introduction

It is urgent to develop the required technologies for swift and economically effective decarbonization of energy [1]. To become useful and cost-effective, the new technologies should be easily upscaled and provide clean dispatchable energy. Furthermore, this energy must be produced at prices comparable to current fossil fuel-based technologies in time to meet the targets of internationally ratified agreements – such as the Paris Agreement, which aims to reduce 43 % of global emissions by 2030 [2]. Hydrogen is the most widely accepted energy vector; its production is often envisioned from water splitting processes (*e.g.*, electrolysis and photoelectrochemical water splitting). Water electrolysis technology is still underdeveloped, and it will take a few years to reach maturity. Moreover, the green power needed for electrolysis is either very expensive or power fluctuates over a day and a year, which, associated with the very high costs of storing hydrogen, makes its implementation more challenging [3,4]. Additionally, current energy and fuel processing infrastructures must be completely changed to fully decarbonize the energy sector. For example, since the 20th century, many energy institutes and companies proposed to blend hydrogen with natural gas for transporting it using the available grid of pipelines [5,6]. However, recovering the hydrogen from natural gas is prohibitively challenging/expensive, considering typical hydrogen fractions found in these blends [7].

Most hydrogen produced currently is obtained by hydrocarbon reforming, *ca.* 78 %, and coal gasification, *ca.* 18 % [8,9]. The most relevant of these processes are methane steam reforming, Eq. (1) [10], methane dry-reforming, Eq. (2) [11], methane partial oxidation, Eq. (3) [12], coal gasification, Eq. (4) [13], and water gas shift reaction, Eq. (5) [14]. Although these processes are yet the most economically competitive, they are responsible for more than 830 Mt of yearly CO_2 emissions, making it impossible to apply them directly for clean hydrogen production. Furthermore, increasing tariffs on CO_2 emissions and demand for carbon credits will gradually decrease their economic viability, even in the industrial setting. Consequently, efforts to eliminate, or alleviate, reforming related CO_2 emissions have been undertaken. Specifically, the capture of CO_2 for subsequent storage or utilization has been considered.

* Corresponding author at: Faculty of Engineering, University of Porto, Rua Dr. Roberto Frias, 4200-465 Porto, Portugal.
E-mail address: mendes@fe.up.pt (A. Mendes).

https://doi.org/10.1016/j.fuel.2024.133115
Received 4 June 2024; Received in revised form 24 August 2024; Accepted 10 September 2024
Available online 14 September 2024

Nomenclature

X_{CH4}	methane conversion
x_{H2}	hydrogen molar fraction
x_{CH4}	methane molar fraction
a_{H2}	hydrogen production activity, $g_{H2} \bullet g_{Ni}^{-1} \bullet h^{-1}$
W	catalyst mass, g_{Ni}
$\dot{m}_{H2}$	hydrogen mass flow, $g_{H2} \bullet h^{-1}$
ρ_{H2}	hydrogen NPT density, $g_{H2} \bullet ml^{-1}$
$F_{CH4,in}$	methane inlet flow, $ml \bullet min^{-1}$
F_{H2}	hydrogen flow, $ml \bullet min^{-1}$
t	time on stream
h	deactivation rate, $g_{H2} \bullet g_{Ni}^{-1} \bullet h^{-2}$
d	average crystal size, nm
k	crystallite shape factor
λ	wavelength, nm
β	full width at half maximum, rad
θ	diffraction angle, rad

Abbreviations:

CMS	catalytic methane splitting
NTP	normal temperature and pressure
BET	Brunauer-Emmett-Teller
SEM	scanning electron microscopy
AFM	atomic force microscopy
XRD	x-ray diffractometry
FWHM	full width at half maximum
DFT	density functional theory

Carbon capture can indeed have a considerable impact on reducing emissions, capturing up to 90 % of CO_2 using absorption processes or even higher for other technologies (*e.g.* membranes, pressure swing adsorption) [15]. However, this decrease in emissions also causes an increase in costs, which has hindered the widespread adoption of carbon capture technologies [9].

$$CH_4(g) + H_2O(g) \rightarrow 3H_2(g) + CO(g), \ \Delta H^0 = 206.2\,kJ \bullet mol^{-1} \quad (1)$$

$$CH_4(g) + CO_2(g) \rightarrow 2H_2(g) + 2CO(g), \ \Delta H^0 = 247\,kJ \bullet mol^{-1} \quad (2)$$

$$CH_4(g) + \frac{1}{2}O_2(g) \rightarrow 2H_2(g) + CO(g), \ \Delta H^0 = -72\,kJ \bullet mol^{-1} \quad (3)$$

$$C_nH_m(coal) + nH_2O(g) \rightarrow \left(n + \frac{m}{2}\right)H_2(g) + nCO(g), \ \text{Endothermic} \quad (4)$$

$$CO(g) + H_2O(g) \rightarrow CO_2(g) + H_2(g), \ \Delta H^0 = -41.09\,kJ \bullet mol^{-1} \quad (5)$$

As the mainstream reforming processes are yet to decarbonize economically, other processes must be considered to produce cost-effective decarbonized hydrogen, while avoiding an abrupt overhaul of the energy sector. Methane splitting is a good candidate to ease the energy transition as it can use the whole natural gas infrastructure for producing locally dispatchable hydrogen. The methane splitting reaction:

$$CH_4 \rightleftharpoons 2H_2 + C(s), \ \Delta H^0 = 75.6\,kJ \cdot mol^{-1} \quad (6)$$

is moderately endothermic and, at low temperatures, no secondary reactions were found – it is then a 100 % selective reaction [16]. Carbon is the only by-product, contrasting with hydrocarbon reforming and coal gasification [17,18]. Due to the high binding energy between carbon and hydrogen atoms, catalytic materials, such as transition metals (Ni, Fe, Co), must be used to perform the reaction at more moderate conditions: 450–800 °C [19,20]. Currently, catalytic methane splitting (CMS) is critically hindered by carbon formation, which grows in and around catalytic particles, deactivating them and clogging reactors [21]. This means that the use of conventional fixed beds, while reported in the literature, is economically unfeasible, as carbon will quickly block the interparticle volume of the bed and stop hydrogen production [22]. Alternatives to fixed beds are also reported, most often fluidized bed reactors, which allow for much more freedom for carbon growth and eventual removal [23]. Molten metal (or molten salt) reactors are also a relevant alternative, which avoids using a solid catalytic bed, substituting it with a liquid medium (*e.g.* Ga, Bi, Sn, NaBr, KBr) with dispersed active metal particles (Ni, Fe, Co) [24,25]. Industrial players, such as the Hazer Group [26] and BASF [27], have also proposed alternatives to the fixed bed systems. Both suggested using moving beds of active but cheap discardable materials namely iron ore and amorphous carbon, respectively, to promote CMS in a continuously renovated catalytic system (continuous bed substitution) operated at high temperatures, between 900 °C and 1400 °C. The moving parts and high operating temperatures are critical hindrances to these systems. Furthermore, specific problems have surfaced in these alternatives, such as defluidization in fluidized systems [28]; carbon clogging on the upper sections of molten metal systems [29]; scale-up limitations in the moving bed systems, related to the excessive volume of moving solids; and an inability to fully separate and isolate carbon by-product in all scenarios.

A different route to tackle hydrogen production from CMS is the substitution of catalytic beds with catalytic films, which can provide catalytic active sites and allow considerable free volume for carbon allotrope growth while avoiding movement of solids or liquids during the process, which is energy-consuming and increases the process complexity. These types of catalytic systems, as they provide room for carbon to grow, also make carbon particle recovery easy, as carbon grows on a film instead of inside a compact matrix. If the interface carbon particle/catalyst is broken, the carbon particles will fall off the catalytic layers. This can be achieved by promoting the reverse reaction to the methane splitting – carbon methanation, as described elsewhere [9]. This work studies the hydrogen production performance of Ni-based films with different morphologies and designs: Ni foil, Ni particles deposited on tubular α-Al_2O_3 porous substrate, supported Ni catalysts of Ni/SiO_2-Al_2O_3 deposited on tubular α-Al_2O_3 porous substrate, Ni particles deposited on carbon felt substrate, and Ni/SiO_2-Al_2O_3 deposited on carbon felt substrate.

2. Materials and methods

2.1. Catalytic layer preparation

Ni foils of 15 cm^2 (130 mg, 9 $mg \cdot cm^{-2}$), rolled around a dense steel tube with 6.35 mm in diameter (1/4′ standard outer diameter), were loaded in a tubular steel reactor. One foil was used as purchased, while a second one was left in *aqua regia* for 12 h at room temperature. *Aqua regia* solution was prepared by mixing 5 ml of 65 % HNO_3 solution dropwise into 30 ml of 37 % HCl solution. The *aqua regia* treated foil was then washed in deionized water before being dried overnight at 120 °C.

NiO and NiO/SiO_2–Al_2O_3 powders were dispersed in α-terpineol to produce emulsions with a solid mass content of 30 %, for dip-coating α-Al_2O_3 membranes. The mixtures were then milled in a Retsch PM 100 ball miller for 1 h at 300 rpm until homogeneous viscous emulsions were formed. The milling procedure was performed with 18 mm diameter zirconia balls, in a sealed 50 ml zirconia vial filled 2/3 with the mixture (and the balls) and 1/3 with atmospheric air, at room conditions. Tubular α-Al_2O_3 membranes with 15 cm^2 exposed geometric area were used to deposit the catalysts, on the shell side of the substrate. The ceramic substrates were dipped in each emulsion for 10 s. Dip-coated

substrates were dried overnight at 200 °C, under constant horizontal rotation, to evaporate the solvent and ensure a homogeneous catalytic layer. The loading of the NiO layer was 150 mg (120 mg of Ni, 8 $mg{\cdot}cm^{-2}$), while the loading of NiO/SiO_2-Al_2O_3 was 310 mg (150 mg of Ni, 10 $mg{\cdot}cm^{-2}$).

NiO and NiO/SiO_2–Al_2O_3 powders were also dispersed in ethylene glycol to produce emulsions with a solid mass content of 10 %, for dip-coating carbon felt. The mixtures were then milled in a Retsch PM 100 ball miller, for 1 h at 200 rpm, until homogeneous viscous emulsions formed. The milling procedure was performed with 5 mm diameter steel balls, in a sealed 10 ml steel vial filled 2/3 with the mixture (and the balls) and 1/3 with atmospheric air, at room conditions. A carbon felt sheet with 15 cm^2 exposed geometric area and 0.6 mm thickness was used to deposit the supported catalyst. The carbon felt was pre-treated at 400 °C, under running dry air, for 12 h. The carbon substrates were dipped in the emulsions for 60 s and then dried overnight at 200 °C, to evaporate the solvent and ensure a homogeneous catalyst layer. The deposited NiO film had a dry load of 180 mg (140 mg of Ni, 9 $mg{\cdot}cm^{-2}$). The deposited NiO/SiO_2-Al_2O_3 film had a dry load of 270 mg (135 mg of Ni, 9 $mg{\cdot}cm^{-2}$).

The choice of solvents and solid contents for the dip-coating was related to the viscosity of the emulsions required to achieve catalyst (Ni) loadings in the range of 9 $mg{\cdot}cm^{-2}$ (area normalized loading of the foil used). The effect of paste composition on the dried substrate's loading was assessed experimentally for each substrate. α-terpineol was used for depositions on α-Al_2O_3 membranes due to its higher viscosity (160 cP at 20 °C according to the supplier) needed to form relatively thick films on a smooth surface. Ethylene glycol (18.4 cP at 20 °C according to the supplier) was used in the high-area carbon felt to form thinner films over the carbon fibers. Table 1 shows the empirical relation between the emulsion composition, with α-terpineol and with ethylene glycol and the dry loading on α-Al_2O_3 and carbon felt, respectively.

Ni foils were purchased from Sigma-Aldrich. 37 % HCl solution was purchased from VWR Chemicals. 65 % HNO_3 solution was purchased from VWR Chemicals. NiO powder, 400 mesh, was purchased from Alfa Aesar. NiO/SiO_2-Al_2O_3 powder, with 62 wt% of Ni and 4:1 SiO_2-Al_2O_3 ratio, was purchased from Sigma-Aldrich. α-terpineol was purchased from Acros Organics. Tubular α-Al_2O_3 membranes were purchased from Inopor. Carbon felt SIGRACET ECM80 was purchased from SGL Carbon.

2.2. Activity evaluation

All catalysts were reduced *in situ* in an atmosphere of 50 % H_2 in N_2, at 550 °C and 1 bar (100 $ml{\cdot}min^{-1}$ total flow), for 1 h, to promote the formation of Ni^0 crystals. The catalyst was previously heated at 1 $°C{\cdot}min^{-1}$, under a flow of 100 $ml{\cdot}min^{-1}$ of N_2. CMS was promoted by feeding 100 $ml{\cdot}min^{-1}$ of methane to the catalytic systems, corresponding to an hourly space velocity of 40 $l_{CH4}{\cdot}g_{Ni}^{-1}{\cdot}h^{-1}$ (reactor is operating in chemical regime). The gas composition was determined, every 2 s, using a mass spectrometer Pfeiffer OmniStar GSD 301O2. The catalytic performance was assessed based on the methane conversion and on the hydrogen production activity, Eqs. (7) and (8), respectively.

$$X_{CH4} = \frac{x_{H2}}{x_{H2} + 2x_{CH4}} \tag{7}$$

$$a_{H2} = \frac{\dot{m}_{H2}}{W} = 60\frac{F_{H2}\rho_{H2}}{W} = 60\frac{2F_{CH4,in}X_{CH4}\rho_{H2}}{W} \tag{8}$$

where X_{CH4} is methane conversion, x_{H2} is hydrogen molar fraction, x_{CH4} is methane molar fraction, a_{H2} is hydrogen production activity in $g_{H2}{\cdot}g_{Ni}^{-1}{\cdot}h^{-1}$, $\dot{m}_{H2}$ is produced hydrogen mass flowrate in $g_{H2}{\cdot}h^{-1}$, W is the catalyst (Ni phase) mass in g_{Ni}, F_{H2} is the produced hydrogen volume flowrate at normal temperature and pressure (NTP) conditions in $ml{\cdot}min^{-1}$, ρ_{H2} is hydrogen density at NTP conditions in $g_{H2}{\cdot}ml^{-1}$ and $F_{CH4,\ in}$ is the methane inlet volume flow at NTP conditions in $ml{\cdot}min^{-1}$.

Deactivation rates, between 2 given moments (i, and j), were assessed through Eq. (9):

$$\text{Deactivation rate} = \frac{a_{H2,i} - a_{H2,j}}{t_j - t_i} \tag{9}$$

where deactivation rate is expressed in activity units$\cdot h^{-1}$ ($g_{H2}{\cdot}g_{Ni}^{-1}{\cdot}h^{-2}$), $a_{H2,i}$ and $a_{H2,j}$ are hydrogen production activities in $g_{H2}{\cdot}g_{Ni}^{-1}{\cdot}h^{-1}$, at moments t_i and t_j in h, respectively.

2.3. Morphological characterization

The textural properties of the particulate catalysts (surface area, pore volume, and average pore size) were retrieved by the cryogenic nitrogen adsorption/desorption method and determined by multi-point Brunauer-Emmett-Teller (BET, Quantachrome Autosorb AS-1) at –196 °C. The samples were pre-outgassed under vacuum conditions at 200 °C for 4 h.

The morphology of catalysts was assessed by scanning electron microscopy (SEM), before and after exposition to methane splitting conditions, in a Phenom XL Desktop Microscope. All micrographs were captured under high vacuum with an electron beam energy of 15 kV. The surface topography of the studied Ni foils was further evaluated through atomic force microscopy (AFM), in a Veeco AFM multimode Nanoscope (IV) MMAFM-2. The samples were analyzed with no prior treatment at a probe lift of 75 nm.

The crystal structure of pristine and used catalysts, as well as produced carbon structures, was studied with X-ray diffraction (XRD) analysis, in a Diffractometer Rigaku Smartlab. Powder samples were irradiated with 1.5406 Å monochromatic radiation, from a Cu Kα source, at angles (2θ) between 20° and 80°, with a step of 0.02°. The resulting diffractograms were compared with database standards (ICDD), allowing the identification of the crystal phases present in each sample. Average crystal size was assessed through Scherrer equation, Eq. (10):

$$d = \frac{k\lambda}{\beta\cos\theta} \tag{10}$$

where d is the average crystal size in nm, k is crystallite shape factor (adimentional), λ is the wavelength of the diffracted X-rays in nm, β is the full width at half maximum (FWHM) in rad, and θ is the diffraction angle in rad. k was given a set value of 0.94 for the characterized materials.

Ab initio calculations were performed at the gamma-point on a ~800 atoms Ni nanoparticle using VASP code [30–32]. The PBE [33] exchange and correlation functional was used and Kohn-Sham orbitals were expanded in a plane wave basis set with an energy cutoff of 400 eV.

Table 1
Empirical relationship between solid contents of catalyst pastes and dry loading on substrates.

Solid content on α–terpineol	10 %	30 %	50 %
Dry-loading on α–Al_2O_3	3–5 $mg{\cdot}cm^{-2}$	7–11 $mg{\cdot}cm^{-2}$	20–25 $mg{\cdot}cm^{-2}$
Solid content on ethylene glycol	**1 %**	**10 %**	**20 %**
Dry-loading on carbon felt	0.5–1 $mg \cdot cm^{-2}$	7–10 $mg{\cdot}cm^{-2}$	Flooded

Table 2
Summary of all systems used for catalytic methane splitting – properties and performance parameters.

System	Material	Specific area $m^2 \cdot g^{-1}$	Substrate	Loading $mg \cdot cm^{-2}$	Thickness µm	Peak activity $g_{H2} \cdot g_{Ni}^{-1} \cdot h^{-1}$	Deactivation rate $g_{H2} \cdot g_{Ni}^{-1} \cdot h^{-2}$	Total productivity $g_{H2} \cdot g_{Ni}^{-1}$
a	Ni foil	Low	–	9	9	0.004	0.020	~0
b	Ni foil (acid)	Low	–	9	~9	0.004	0.020	~0
c	Ni-bulk	4.87	α-Al_2O_3	8	~15	0.14	0.52	0.011
d	Ni/SiO_2-Al_2O_3	130	α-Al_2O_3	10	~30	1.2	0.020	40
e	Ni-bulk	4.87	Carbon felt	9	Sub monolayer	1.5	6.0	0.095
f	Ni/SiO_2-Al_2O_3	130	Carbon felt	9	Sub monolayer	0.90	0.011	40

3. Results and discussion

3.1. Activity assessment and scanning electron microscopy imaging

Methane splitting was performed at 550 °C over the various catalytic films by feeding the reactor with 100 $ml \cdot min^{-1}$ of methane at atmospheric pressure. A summary of all the systems used for CMS is provided in Table 2, indicating the main properties of the used systems (catalytic material, specific area of catalyst, used substrate, specific mass loading of catalyst, and film thickness), as well as the most relevant catalytic performance parameters (peak catalytic activity, deactivation rate, and total Ni-normalized hydrogen productivity).

The first experiment, system *a*, was performed using an as-purchased Ni sheet, and the results are shown in Fig. 1A1 (close-ups in A2 and A3), revealing a very low hydrogen catalytic activity, a_{H2}, at the set operation conditions – <0.004 $g_{H2} \cdot g_{Ni}^{-1} \cdot h^{-1}$ (<0.1 % conversion). Such a result was expected, as the Ni sheet presents a very small specific area, as illustrated in Fig. 2A. Furthermore, it is widely accepted that catalytic methane decomposition is structure-sensitive, when promoted over transition metals, requiring specific Ni sites to decompose methane [34] and diffuse and nucleate carbon [35]. Ni foils are formed by large and highly ordered Ni granules, with an average crystal diameter ≫100 nm (assessed through XRD, *cf.* next section). Poorly coordinated Ni atoms, such as those of stepped surfaces or kinks, are particularly rare in such large crystallites [36]. This uniformity in exposed crystal planes hinders the movement of carbon atoms [37], making the nucleation of carbon allotropes more challenging [38]. The distribution of crystal domains is further investigated in the next section based on X-ray diffraction. Fig. 2B displays SEM images of the Ni sheet after the reaction, showing a slight increase in surface rugosity compared to the pristine material. A second Ni sheet (identical to the first one) was treated in *aqua regia* to generate surface defects – system *b*. These defects are expected to increase specific area (higher roughness) and the dispersion of catalytic planes, such as stepped surfaces and edge planes. As seen in Fig. 2C, the acid bath successfully increases the surface roughness, increasing the exposed area and generating sharp edges on the Ni crystals. Despite these surface changes, the catalytic activity only slightly increased, experiment *b*, illustrated in Fig. 1A1 (close-ups in A2 and A3) – still below 0.004 $g_{H2} \cdot g_{Ni}^{-1} \cdot h^{-1}$ (<0.1 % conversion). The negligible increase in the catalytic activity was attributed to the sintering of Ni at test conditions, as observed in Fig. 2D. The enhanced area and exposed planes gave way to large Ni particles, which suffer from the same problems as the untreated Ni sheet: small active area and low distribution of surface defects.

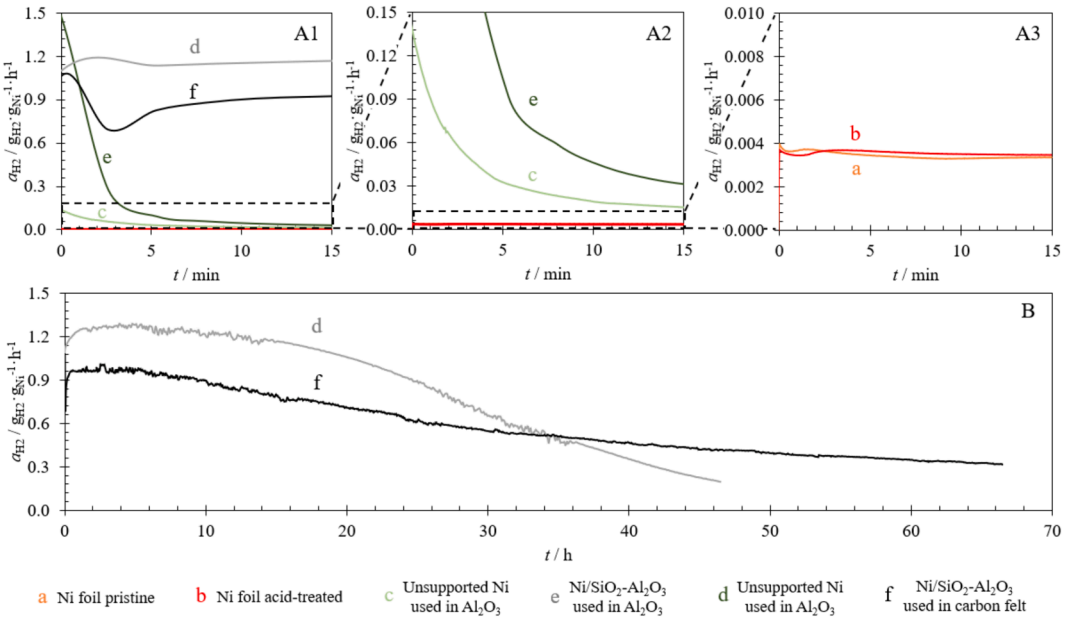

Fig. 1. Catalytic methane splitting activity of a) pristine Ni foil (orange); and b) acid treated Ni foil (red); c) reduced NiO film deposited on the shell-side of tubular α-Al_2O_3 membranes (light green); d) NiO/SiO_2-Al_2O_3 film deposited on the shell-side of tubular α-Al_2O_3 membranes (grey); e) reduced NiO deposited on carbon felt (dark green); and f) NiO/SiO_2-Al_2O_3 deposited on carbon felt (black). A – 15 min of time-on-stream; B – after a few hours of time-on-stream. (For interpretation of the references to colour in this figure legend, the reader is referred to the web version of this article.)

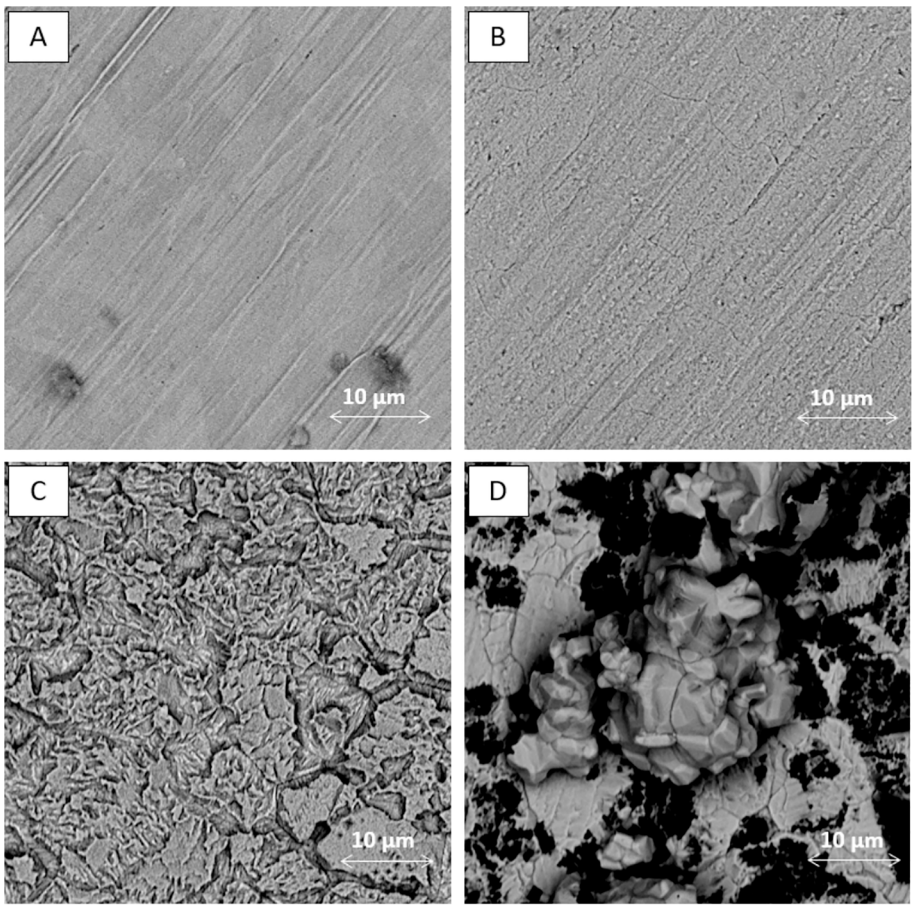

Fig. 2. Scanning electron microscopy micrographs (backscattered electron detector) of Ni sheets: A – pristine sheet; B – after reaction pristine sheet; C – acid treated sheet; D – after reaction on the acid treated sheet.

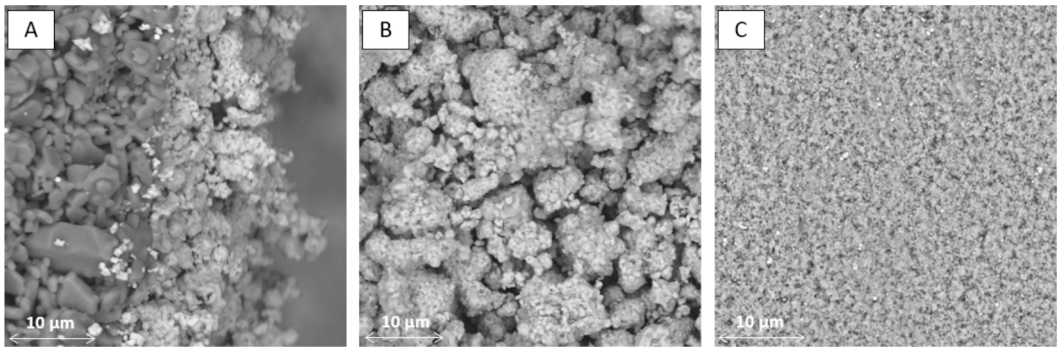

Fig. 3. Scanning electron microscopy micrographs (backscattered electron detector) of system *c* – reduced *in situ* NiO layer: A – cross-section view; B – top view; C – after reaction, top view.

The third experiment, system *c*, uses a catalytic film of NiO particles, which were reduced *in situ* under the same conditions as the Ni foils – 550 °C and H_2:N_2 gas mixture with 50 % hydrogen. The catalytic film was prepared from microstructured NiO particles (1–10 µm), which, after reduction, created the rough and porous layer observed in Fig. 3A and Fig. 3B, with thicknesses between 10 µm and 20 µm; the catalyst activity of this film is shown in Fig. 1A1 (close-up in A2). The catalytic activity onset presented a higher value – *ca.* $0.14 \cdot g_{H2} \cdot g_{Ni}^{-1} \cdot h^{-1}$ (2.5 % conversion) – than the foils but the catalyst deactivates quickly – *ca.* $0.52\ g_{H2} \cdot g_{Ni}^{-1} \cdot h^{-2}$ deactivation rate along the 15 min experiment. The observed pores and roughness represent a major increase in the specific area – *ca.* 4.87 $m^2 \cdot g^{-1}$ – obtained by nitrogen physisorption, contributing to enhanced hydrogen production. Furthermore, the smaller size of the crystallites – corrected full width at half maximum (FWHM) of XRD peaks of reduced Ni particle film was 10 fold that of the foils – contributes to a higher number of edge and step atoms around the particles [39]. These surface sites should contribute to favorable methane splitting mechanisms, further justifying the increased activity [34]. The deactivation was mostly assigned to the clogging of the catalytic film – loss of exposed active area of the film, which became completely compacted with carbon, as seen in Fig. 3C. A total of *ca.* $0.011\ g_{H2} \cdot g_{Ni}^{-1}$ (*ca.* $0.032\ g_C \cdot g_{Ni}^{-1}$) were produced.

The fourth experiment uses a catalytic layer of aluminosilicate supported nickel nanoparticles (Ni/SiO_2-Al_2O_3); the Ni nanoparticles are stabilized by the support, generating a high specific area – *ca.* 130 $m^2 \cdot g^{-1}$ – obtained by nitrogen physisorption. Additionally, the

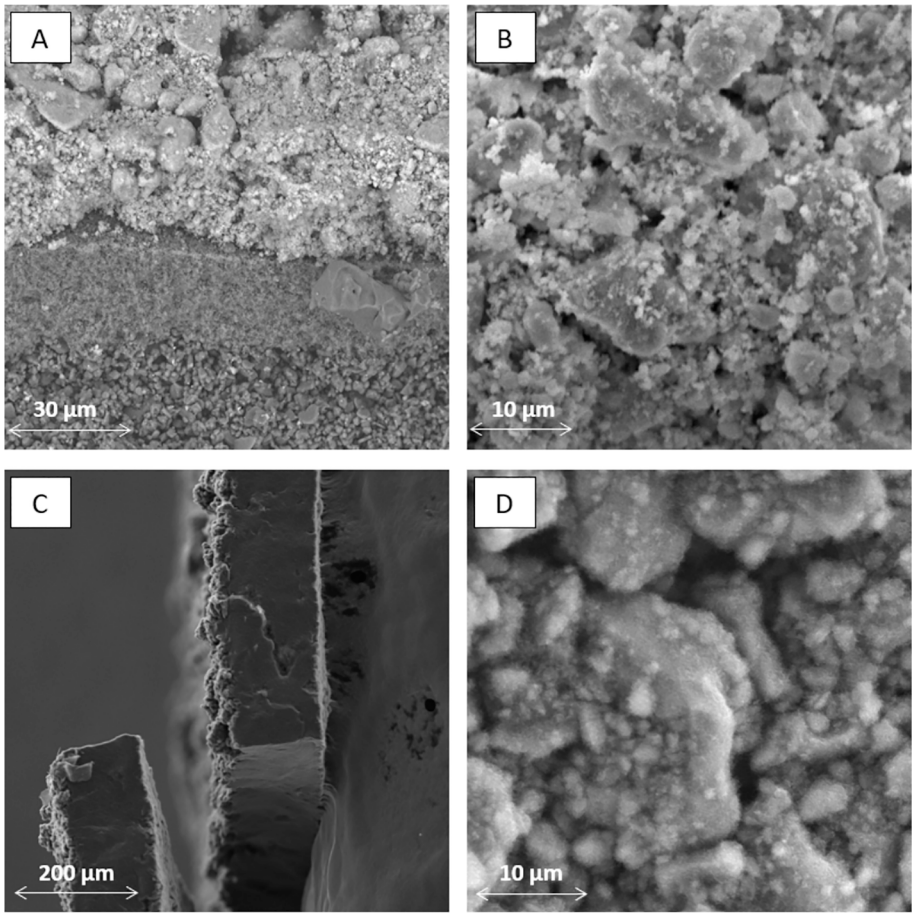

Fig. 4. Scanning electron microscopy micrographs of system *d* – SiO_2-Al_2O_3-supported Ni composite film, deposited on tubular α–Al_2O_3 membrane: A – cross-section view (backscattered electron detector); B – top view (backscattered electron detector); C – after 46.5 h reaction cross-section view (secondary electron detector); D – after 46.5 h reaction top view (backscattered electron detector).

macrostructure of the catalytic layer will be mainly dictated by the substrate. When deposited on tubular α–Al_2O_3 membranes, this catalyst originated a very high catalytic activity, experiment *d*, as seen in Fig. 1A1. The pristine catalytic layer, deposited on the tubular α–Al_2O_3 membrane, can be observed in Fig. 4A (cross-section view) and Fig. 4B (top view), showing a catalytic layer with *ca.* 30 µm thickness, with Ni nanoparticles with 10 nm average crystallite size (assessed by Scherrer equation, *cf.* next section), spread throughout the ceramic support. Unlike the reduced unsupported NiO film, which got clogged with carbon, the Ni nanoparticles have more free volume around them. This additional volume allows the reaction to progress further, before the formed carbon occupies all the initially available space. Stable activity was maintained throughout the initial 15 min operation window – 1.2 $g_{H2}{\cdot}g_{Ni}^{-1}{\cdot}h^{-1}$ (19 % conversion). Moreover, the composite catalytic layer expanded with carbon formation, creating a porous sheet of carbon and catalyst, as seen in Fig. 4C (cross-section view) and D (top view), allowing the reaction to proceed much longer; a stable methane splitting reaction rate was maintained for tens of hours, as observed in Fig. 1B. Further, no signs of reactor clogging were detected through the entire experiment. Even so, the active layer was progressively destroyed during the reaction, making it impossible to regenerate the catalyst and recover the carbon product without stopping the process. The reaction was stopped after 46.5 h, when catalytic activity dropped to *ca.* 15 % of its maximum value (0.20 $g_{H2}{\cdot}g_{Ni}^{-1}{\cdot}h^{-1}$, 3.5 % conversion), resulting in an overall deactivation rate of 0.020 $g_{H2}{\cdot}g_{Ni}^{-1}{\cdot}h^{-2}$. A total of *ca.* 40 $g_{H2}{\cdot}g_{Ni}^{-1}$ (120 $g_{C}{\cdot}g_{Ni}^{-1}$) were produced.

Pathways for carbon growth and eventual removal (regeneration) should be provided to achieve a structurally stable catalytic layer. Depositing the catalytic material (with the previously applied catalyst loadings) over a smooth surface, such as the tubular α-Al_2O_3 membranes, will always result in a packed layer, which will either clog or disintegrate with carbon growth. Decreasing catalyst loading (mass of Ni per geometric area) may alleviate this issue, but the accompanying decrease in power density hinders the industrial prospects of the catalytic methane splitting systems. Alternatively, the use of macrostructured substrates should allow high catalyst loadings while avoiding the packing of the catalyst particles. Fig. 5A and B display SEM micrographs of unsupported NiO deposited on the 0.6 mm thick carbon felt, system *e*. While the normalized catalyst loading is similar to the previous experiments, the catalyst particles are not heavily stacked over each other in any given carbon fiber. This particle distribution was expected to allow a more stable activity without clogging the catalytic film so easily. Fig. 1A, experiment *e*, shows the unsupported Ni deposited on carbon felt, which displays much higher catalytic activity – *ca.* 1.5 $g_{H2}{\cdot}g_{Ni}^{-1}{\cdot}h^{-1}$ (20 % conversion) – than the same catalyst when deposited on α-Al_2O_3 substrate (2.5 % conversion). However, the deactivation rate was also faster, displaying an overall deactivation rate, along the 15 min of the experiment, of *ca.* 6.0 $g_{H2}{\cdot}g_{Ni}^{-1}{\cdot}h^{-2}$. Fig. 5C and D display the Ni-deposited carbon felt substrate, showing a reduction in the density of Ni particles and average particle size. This indicates that carbon growth is breaking the metal particles and possibly causing them to be removed from the substrate. As such, the used bulk-Ni is not suitable to catalyze methane splitting – the change in macrostructure eases the contact between gas and solid phase, increasing the catalytic activity, but the catalyst was not morphologically stable. A total of *ca.* 0.095 $g_{H2}{\cdot}g_{Ni}^{-1}$ (*ca.* 0.29 $g_{C}{\cdot}g_{Ni}^{-1}$) were produced.

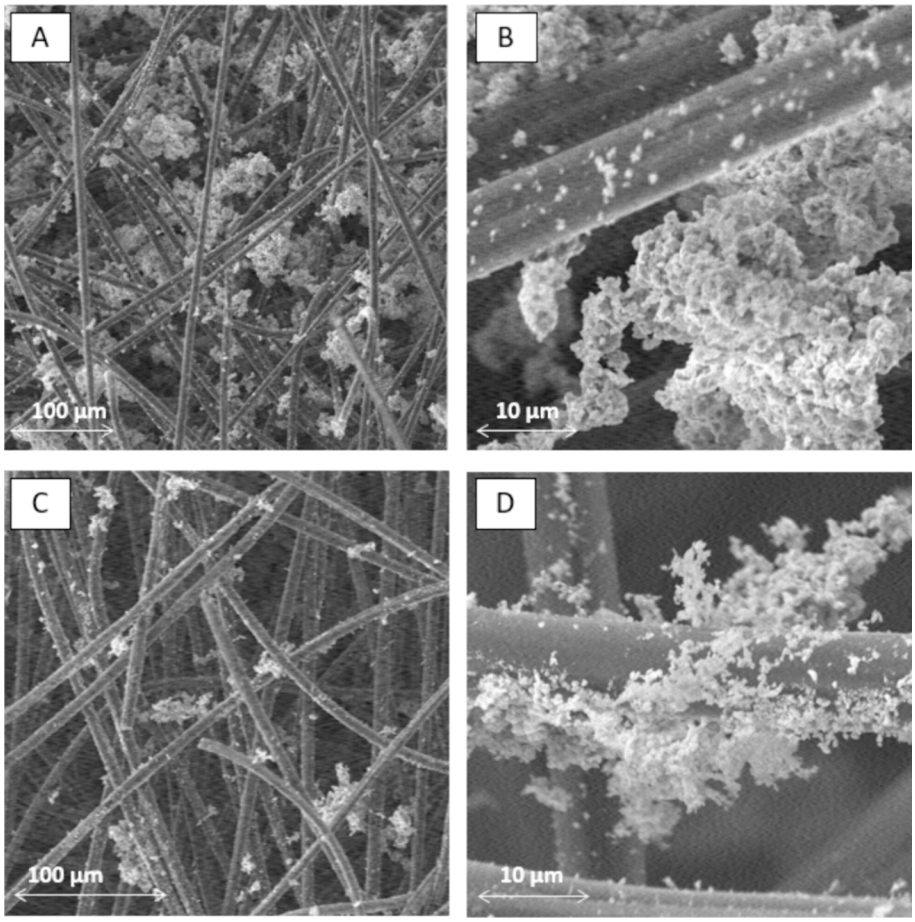

Fig. 5. Scanning electron microscopy images of system *e* – unsupported bulk-Ni film: A – catalyst deposition over carbon felt fibers; B – close-up on deposited carbon felt fiber; C – deposited carbon felt after 15 min reaction; D – close-up on deposited carbon felt after 15 min reaction.

Fig. 6A and B display SEM micrographs of Ni/SiO_2-Al_2O_3 deposited on the 0.6 mm thick carbon felt, system *f*. The catalyst particles are smaller than the previous NiO, resulting in a more well-dispersed catalytic layer. This particle dispersion was expected to allow a more stable activity without destroying the catalytic film. In Fig. 1B, experiment *f*, the Ni/SiO_2-Al_2O_3-loaded carbon felt is initially less active than the tubular Ni/SiO_2-Al_2O_3-loaded α–Al_2O_3 membrane – 0.9 $g_{H2}\ g_{Ni}^{-1}\ h^{-1}$ (15 % conversion), but with the time-on-stream, the α–Al_2O_3 system starts to deactivate more rapidly. The experiment using carbon felt substrate was left running for 66.5 h, reaching a hydrogen production of *ca.* 40 $g_{H2}{\cdot}g_{Ni}^{-1}$ (*ca.* 120 $g_C{\cdot}g_{Ni}^{-1}$), equating the film deposited on α–Al_2O_3. At the 66.5 h mark, it was seen that the activity was *ca.* 30 % of its maximum value during this experiment (*ca.* 0.32 $g_{H2}{\cdot}g_{Ni}^{-1}{\cdot}h^{-1}$, 5.5 % conversion), resulting in an overall deactivation rate of *ca.* 0.011 $g_{H2}\ g_{Ni}^{-1}{\cdot}h^{-2}$. Furthermore, the deactivation rate at the end of the experiment (calculated with the last 5 h of time-on-stream for each experiment) was much lower than that of the film deposited on α–Al_2O_3 – 0.004 $g_{H2}{\cdot}g_{Ni}^{-1}{\cdot}h^{-2}$ *vs* 0.022 $g_{H2}{\cdot}g_{Ni}^{-1}{\cdot}h^{-2}$. This indicates that the expected increase in stability was achieved after producing the same amount of hydrogen and carbon. When analyzing the post-reaction film, Fig. 6C and D, it is observed that the catalyst does not remain attached to the fibers of the carbon felt. However, in contrast to the NiO-deposited carbon felt, the catalyst particles remain within the substrate, producing carbon chunks that remain enclosed in the felt. Neither the carbon chunks nor the catalyst particles are bonded to the substrate, instead they are entangled in the middle of the fibers.

3.2. Atomic force microscopy and X-ray diffractometry

The exposed surface of the catalytic layers and the active crystal planes were further studied using atomic force microscopy (AFM) on the Ni foils and X-ray diffractometry (XRD). Fig. 7 presents the AFM measurements of the Ni foils. Microscopic roughness is observed in the pristine Ni foil (Fig. 7A) with surface granules of 200–500 nm diameter. These granules are much bigger than the generally accepted optimal particle size range for CMS systems, helping to justify the lack of activity of the foil [17]. After the reaction, the formation of very long (few µm length) orientated structures is observed – Fig. 7B (survey AFM micrograph). This indicates a reorganization of the structure of the material at a microscopic level, implying a significant level of freedom of movement for Ni atoms, under the applied methane splitting operating conditions. After this restructuring, the material displays a similar degree of roughness to the pristine foil – it shows big granules with a small specific surface area. On the other hand, the acid treatment promoted the formation of surface particles with a very broad particle size distribution, as shown in Fig. 7C. The smaller particles, with *ca.* 20 nm, should present a high specific area, as well as a large dispersion of edge and stepped sites, which should contribute to an increased hydrogen production activity [40]. After exposure to the methane splitting conditions, the acid treated foil shows the collapse of its initial morphology, *cf.* Fig. 7D. The foil became very smooth, compared to the pristine foil, displaying a few large particles of *ca.* 600 nm, scattered over the surface. This smooth surface and the coalesced particles are very different from the morphology promoted by the acid treatment, justifying the underwhelming catalytic activity reported (activity is maximized in smaller particles).

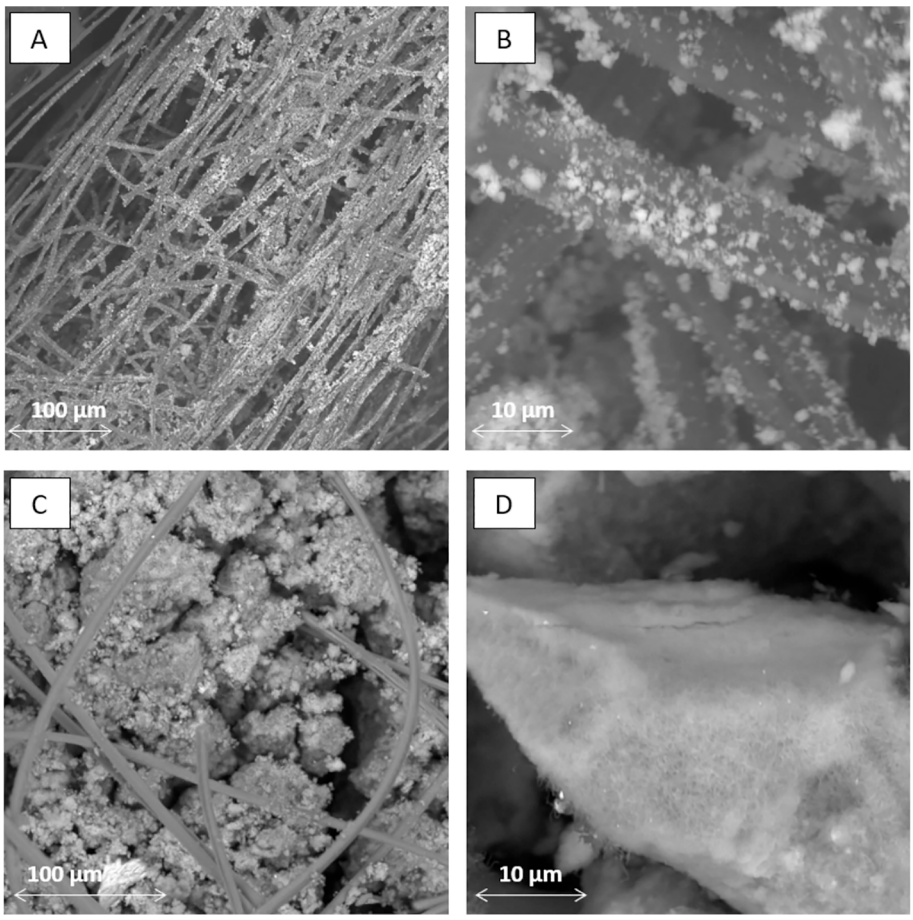

Fig. 6. Scanning electron microscopy images of system *f* – SiO_2-Al_2O_3-supported Ni composite film: A – catalyst deposition over carbon felt fibers; B – close-up on deposited carbon felt fiber; C – deposited carbon felt after 66.5 h reaction; D – close-up on deposited carbon felt after 66.5 h reaction.

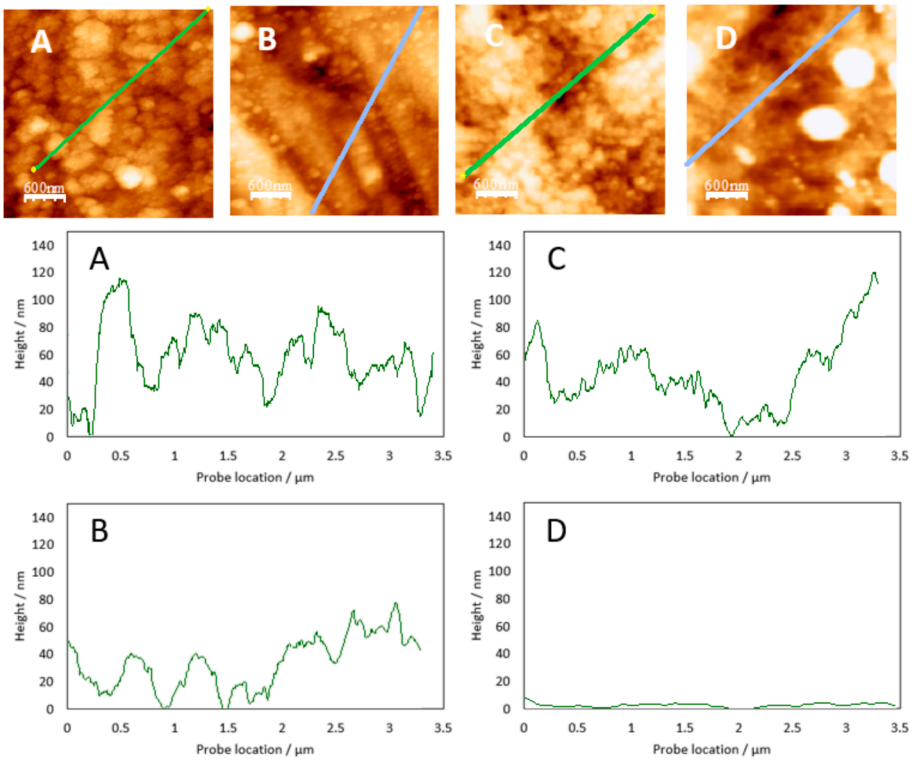

Fig. 7. Atomic force microscopy measurements of A – pristine Ni foil, B – used Ni foil, C – acid treated Ni foil, and D – used acid treated Ni foil.

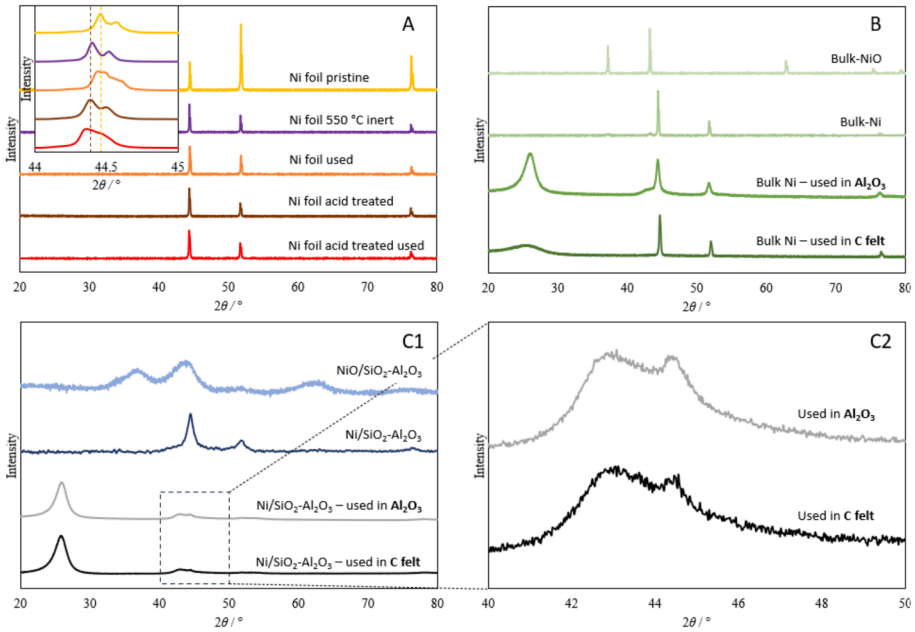

Fig. 8. X-ray diffractograms of A – Ni foils; B – unsupported Ni films; C1 – supported Ni films; and C2– zoom-in on used supported Ni films.

Fig. 8A shows the XRD diffractograms obtained from the metal foils. 5 Ni foils were characterized: i) pristine Ni foil (as purchased); ii) Ni foil heated up to 550 °C in an inert atmosphere; iii) Ni foil used for CMS; iv) Ni foil treated in *aqua regia*; and v) Ni foil treated in *aqua regia* used for CMS. In all samples, only the Ni phase (ICDD 00-004-0850) was identified; the intensity was normalized by the (111) peak intensity for all characterized foils. All foils generate diffractograms with very sharp peaks, with full width at half maximums (FWHM) comparable to the LaB_6 reference, *i.e.* a very large average crystal size. As seen in the AFM micrographs, this indicates excessively large Ni particles unfavorable in catalyzing methane splitting. The pristine foil displays the most intense diffraction peak at 51.8° – corresponding to the (100) plane – that suggests a specific crystal orientation favoring diffractions at this plane, with a *ca.* 2.34 (100)/(111) intensity ratio. This orientation changed when either high temperature (550 °C, the operative temperature of CMS) or acid conditions were applied, reaching an intensity ratio of 0.54 and 0.45, respectively, which is consistent with regular bulk structure (0.62). This indicates that Ni spontaneously reorganizes at these conditions, with the (111) diffractions being now the most intense. This is in agreement with the AFM micrographs, and both results concur to indicate that promoting specific Ni active sites (nanostructures) over Ni macrostructures is unfeasible for CMS at the applied conditions.

In the case of samples treated at high temperature and with acid, a slight deviation of the peaks towards lower diffraction angles (0.1°) is observed, indicating an expansion of the lattice parameters of the Ni^0 crystals by *ca.* 0.00075 nm. In addition, acid treated or untreated samples exposed to CMS conditions present a complex XRD pattern shape, with peaks showing multiple features or broad profiles (see inset of Fig. 8A for the case of the (1 1 1) plane). The lattice expansion after acid or temperature treatment can (qualitatively) be ascribed to the *ca.* 15 % higher surface tension of the (1 0 0) over (1 1 1) surface, *i.e.* 1.92 $J{\cdot}m^{-2}$ *vs* 2.21 $J{\cdot}m^{-2}$, respectively [41]. Additionally, the interface tension of grain boundaries also depends on the relative surface. The interface tension of *Tilt* $\sum 5$, involving the (1 0 0) plane, is estimated to be sizably higher than *twist* $\sum 3$ and *twist* $\sum 7$, involving the (1 1 1) plane, *i.e.* 1.1 $J{\cdot}m^{-2}$ *vs ca.* 0 $J{\cdot}m^{-2}$ and 0.5 $J{\cdot}m^{-2}$ [42], respectively. Following the Laplace law, for a sample exposed to the same environment, a higher surface/interface tension corresponds to a higher internal pressure, leading to lattice compression. The alteration of orientation induced by acid treatment or temperature, and the ensuing reorganization from mainly (1 0 0) to regular crystallites, reduces the weighted surface tension, resulting in a lattice relaxation. This is indeed consistent with recent results reporting a facet-dependent strain in Pt nanoparticles [43].

Concerning the more complex shape of the XRD pattern upon exposure to CMS conditions, it is speculated that this is related to the embedding of the carbon atom inside the metal nanoparticle. The coordination of C to Ni atoms on Ni (100) is higher than the coordination on the (111), *i.e.* 4 *vs* 3, respectively. Thus, upon reorganization, carbon atoms on the surface become less stable, and density functional theory (DFT) calculations show that its embedding in interstitial positions is favored by *ca.* 0.5 eV. Considering polydispersity in particle size, facets composition, *etc.*, the concentration of embedded carbon atoms can be different from nanoparticle to nanoparticle, which is reflected on their lattice parameter, finally leading to broad and/or multi-featured peaks. Fig. 9 schematizes the computational sample of an 800-atom nanoparticle considered for DFT calculations.

Fig. 8B shows the XRD diffractograms obtained from analyzing unsupported particulate Ni catalyst films before and after reduction, and after methane splitting reaction; all the diffractograms were normalized by their respective highest intensity peak. The initial NiO peaks (ICDD 98-000-5229) were observed to be very sharp, with a FWHM comparable to the LaB_6 reference. This indicates the presence of very big crystallites, akin to those of the Ni foils. After reduction, the identified Ni (ICDD 00-004-0850) peaks are broader than the NiO ones, indicating

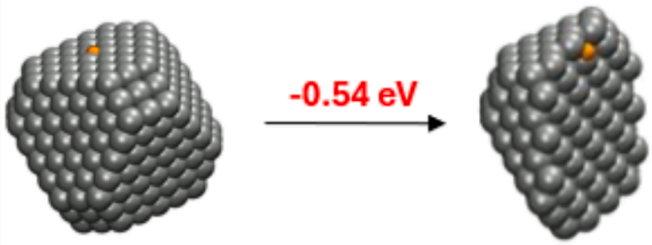

Fig. 9. Computational samples: *ca.* 800 atoms Ni nanoparticle with C on the most stable site of the (111) surface and in the interstitial site inside the metal particle.

that the reduced Ni phase is composed of smaller crystallites. The apparent crystal size of reduced Ni calculated by the Scherrer equation (FWHM corrected with LaB_6 reference) is 170 nm, indicating that these crystals are still quite large. After running the CMS reaction, the particulate Ni layer deposited on α-Al_2O_3 presents a mixture of metallic Ni (ICDD 00-004-0850) and carbon (ICDD 00-058-1638), which is the consequence of the widespread carbon formation inside the pores of the catalytic layer, as previously observed in the SEM images – Fig. 3C. Furthermore, these Ni peaks are broader than observed in the reduced sample, indicating an average crystallite size of *ca*. 18 nm (Scherrer equation). This, again, reinforces the claim that the nickel catalyst self-tunes its morphology under the studied methane splitting operating conditions. This final average crystal size of 18 nm is within the accepted optimal range to promote CMS [9], justifying the much higher catalytic activity than the foils. The diffractogram of Ni deposited on carbon felt displayed a mixture of Ni (ICDD 00-004-0850) and carbon (ICDD 00-058-1638). However a much smaller C:Ni intensity ratio (4:10 *vs* 1:1) was observed, even though the carbon felt system produced much more carbon. Furthermore, the average crystallite size of these Ni particles after CMS was *ca*. 59 nm (Scherrer equation), indicating a less evident self-tunning towards smaller crystalline size. The catalytic activity of the unsupported-Ni deposited on carbon felt decreases with time; this was assigned to the loss of catalyst. As seen in the SEM micrographs, Fig. 5C, catalyst particle density on the carbon felt decreases after the reaction. Also, the carbon clogging observed in the SEM micrographs of α-Al_2O_3-deposited system (Fig. 3C) did not occur when using carbon felt. As such, much of the formed carbon may not be present in the sample, when analyzed by XRD. As smaller Ni particles are accepted to be more active [9], they should produce more carbon and consequently be preferentially dragged with it, justifying the higher average crystallite size coupled with the higher hydrogen and carbon production.

Fig. 8C1 and Fig. 8C2 display the XRD diffractograms from analyzing supported Ni films. It can be seen that the supported Ni catalyst is oxidized at atmospheric conditions (NiO – ICDD 98-000-5229), emphasizing the need for *in situ* reduction before CMS. The observed NiO peaks are very broad, with an average crystal size of *ca*. 2 nm, assessed through the Scherrer equation. After reduction, the obtained Ni (ICDD 00-004-0850) peaks are sharper than the original NiO phase, indicating an increase in average crystal size to *ca*. 8 nm. Ni average crystal size is further increased to *ca*. 12 nm after exposure to methane splitting conditions (further peak sharpening). This average particle size is also within the accepted optimum range, with the supporting structure enhancing catalyst specific area, justifying the very high activities observed in both supported catalyst systems. This increase in crystal size suggests a sintering phenomenon between neighboring crystallites, which contradicts the effects observed in the unsupported Ni system. Consequently, the self-tune of the crystallite size is directed to a specific range of *ca*. 10–20 nm. The average crystallite size of the supported Ni particles was not affected by the substrate, at the applied conditions.

4. Conclusion

Six different nickel-based systems were used to produce hydrogen from catalytic methane splitting at low temperature. Pristine (experiment *a*) and acid treated (experiment *b*) Ni foils display a very low hydrogen production. Using particulate bulk-Ni greatly improved the hydrogen production, but system stability was very low. Bulk-Ni was deposited in α–Al_2O_3 (experiment *c*) and carbon felt (experiment *e*) – catalytic activity dropped more than 90 % after just 15 min of time-on-stream, in both systems. Using SiO_2–Al_2O_3–supported Ni nanoparticles presented the highest hydrogen production and allowed the tunning of the macrostructure without direct impact on the nanostructure. This catalyst was employed in a film deposited over an α–Al_2O_3 tube (experiment *d*) and as discrete particles attached to the carbon fibers of a carbon felt substrate (experiment *f*). It was seen that the stacking of catalyst particles over each other hinders the stability of the system, leading to a gradual decrease in hydrogen productivity. The catalytic layer deposited in the α–Al_2O_3 tube exhibited very high activity. Still, the deactivation rate increased considerably after *ca*. 15 h on stream, with complete detachment of the film from the substrate observed after 46.5 h. In contrast, the carbon felt avoids stacking the catalyst particles and is more stable, although it presents an initial period with less activity. The catalyst on the carbon felt substrate overtook the activity of the catalyst on the α–Al_2O_3 tube substrate after 35 h on-stream. After producing the same relative amount of hydrogen (40 $g_{H2}{\cdot}g_{Ni}^{-1}$), compared to the catalyst on the α–Al_2O_3 substrate, the catalyst on the carbon felt still displayed a higher activity (0.32 $g_{H2}{\cdot}g_{Ni}^{-1}{\cdot}h^{-1}$ *vs* 0.20 $g_{H2}{\cdot}g_{Ni}^{-1}{\cdot}h^{-1}$) and lower deactivation rate (0.004 $g_{H2}{\cdot}g_{Ni}^{-1}{\cdot}h^{-2}$ *vs* 0.022 $g_{H2}{\cdot}g_{Ni}^{-1}{\cdot}h^{-2}$, in the last 5 h on-stream).

Ni atoms display high mobility in all studied systems, restructuring when exposed to methane splitting conditions. In the bulk Ni materials, the macrostructure was shown to affect this restructuring. When exposed to CMS conditions, Ni foils maintain their very large crystallites while eliminating any nanostructure present at the surface. This indicates that bulk Ni materials with well-developed crystallites (≫100 nm) are not appropriate to catalyze the methane splitting reaction. The specific area is naturally very low, and the system restructures into a smooth surface, regardless of any surface nanostructures. For materials with smaller initial Ni crystallites, the metallic Ni was shown to self-tune towards a crystallite range of *ca*. 10–20 nm. This crystal size tunning was not affected by the macrostructure of the catalytic systems.

CRediT authorship contribution statement

Luís Alves: Writing – original draft, Methodology, Investigation, Conceptualization. **Vítor Pereira:** Writing – review & editing, Investigation. **Paula Dias:** Writing – review & editing, Project administration. **Tiago Lagarteira:** Writing – review & editing, Project administration. **Simone Meloni:** Writing – original draft. **Gonzalo Prieto:** Writing – review & editing, Supervision, Project administration. **Adélio Mendes:** Writing – review & editing, Supervision, Funding acquisition.

Declaration of competing interest

The authors declare the following financial interests/personal relationships which may be considered as potential competing interests: [Adelio Mendes has patent #WO2020121287 issued to University of Porto. If there are other authors, they declare that they have no known competing financial interests or personal relationships that could have appeared to influence the work reported in this paper].

Data availability

Data will be made available on request.

Acknowledgments

The authors acknowledge the funding received from the European Union's Horizon 2020 programme - FET Proactive research and innovation action - under grant agreement No. 952219 (project 112CO2). This work was also supported by national funds through FCT/MCTES (PIDDAC): LEPABE, UIDB/00511/2020 (DOI: 10.54499/UIDB/00511/2020) and UIDP/00511/2020 (DOI: 10.54499/UIDP/00511/2020) and ALiCE, LA/P/0045/2020 (DOI: 10.54499/LA/P/0045/2020).

Luís Alves, Vítor Pereira, and Paula Dias acknowledge the Portuguese Foundation of Science and Technology (FCT) support for their grants 2020.10008.BD, SFRH/BD/143218/2019, and CEECIND/02862/2018, respectively. Simone Meloni acknowledges funding under the National Recovery and Resilience Plan (NRRP), Mission 4 Component 1 ("Potenziamento dell'offerta dei servizi di istruzione: dagli asili nido all'Università"), Investment 4.1 "Estensione del numero di dottorati di ricerca e dottorati innovativi per la pubblica amministrazione e il

patrimonio culturale".

The authors also thank the contribution of Nicola Verziaggi, from the Department of Chemical Pharmaceutical and Agricultural Sciences of the University of Ferrara, on the support in computational work and the fruitful discussion.

References

[1] Marques L. In: Capitalism and Environmental Collapse. Cham: Springer International Publishing; 2020. https://doi.org/10.1007/978-3-030-47527-7.
[2] United Nations. The Paris Agreement 2015. https://unfccc.int/process-and-meetings/the-paris-agreement (accessed June 28, 2024).
[3] International Energy Agency. Global Hydrogen Review 2022. OECD; 2022. 10.1787/a15b8442-en.
[4] IRENA. Renewable Energy Statistic 2023. Abu Dhabi: 2023.
[5] IGT Process Research Division. HYGAS: 1964 to 1972. Pipeline gas from coal–hydrogenation (IGT hydrogasification process). Volume 4. vol. 4. Washington, D. C.: 1975. 10.2172/5074193.
[6] Buczyński R, Uryga-Bugajska I, Tokarski M. Recent advances in low-gradient combustion modelling of hydrogen fuel blends. Fuel 2022;328:125265. https://doi.org/10.1016/j.fuel.2022.125265.
[7] Jackson C, Smith G, Kucernak AR. Deblending and purification of hydrogen from natural gas mixtures using the electrochemical hydrogen pump. Int J Hydrogen Energy 2024;52:816–26. https://doi.org/10.1016/j.ijhydene.2023.05.065.
[8] Zhang L, Jia C, Bai F, Wang W, An S, Zhao K, et al. A comprehensive review of the promising clean energy carrier: Hydrogen production, transportation, storage, and utilization (HPTSU) technologies. Fuel 2024;355:129455. https://doi.org/10.1016/j.fuel.2023.129455.
[9] Alves L, Pereira V, Lagarteira T, Mendes A. Catalytic methane decomposition to boost the energy transition: Scientific and technological advancements. Renew Sustain Energy Rev 2021;137:110465. https://doi.org/10.1016/j.rser.2020.110465.
[10] Xu J, Froment GF. Methane steam reforming, methanation and water-gas shift: I. Intrinsic kinetics AIChE J 1989;35:88–96. https://doi.org/10.1002/aic.690350109.
[11] Andraos S, Abbas-Ghaleb R, Chlala D, Vita A, Italiano C, Laganà M, et al. Production of hydrogen by methane dry reforming over ruthenium-nickel based catalysts deposited on Al_2O_3, $MgAl_2O_4$, and YSZ. Int J Hydrogen Energy 2019;44:25706–16. https://doi.org/10.1016/j.ijhydene.2019.08.081.
[12] Dissanayake D, Rosynek MP, Kharas KCC, Lunsford JH. Partial oxidation of methane to carbon monoxide and hydrogen over a Ni/Al_2O_3 catalyst. J Catal 1991;132:117–27. https://doi.org/10.1016/0021-9517(91)90252-Y.
[13] Lin S, Harada M, Suzuki Y, Hatano H. Hydrogen production from coal by separating carbon dioxide during gasification. Fuel 2002;81:2079–85. https://doi.org/10.1016/S0016-2361(02)00187-4.
[14] Holladay JD, Hu J, King DL, Wang Y. An overview of hydrogen production technologies. Catal Today 2009;139:244–60. https://doi.org/10.1016/j.cattod.2008.08.039.
[15] Bose D, Bhattacharya R, Kaur T, Pandya R, Sarkar A, Ray A, et al. Innovative approaches for carbon capture and storage as crucial measures for emission reduction within industrial sectors. Carbon Capture. Sci Technol 2024:12. https://doi.org/10.1016/j.ccst.2024.100238.
[16] Ashik UPM, Wan Daud WMA, Ichiro Hayashi J. A review on methane transformation to hydrogen and nanocarbon: Relevance of catalyst characteristics and experimental parameters on yield. Renew Sustain Energy Rev 2017;76:743–67. https://doi.org/10.1016/j.rser.2017.03.088.
[17] Hamdan M, Halawy L, Abdel Karim Aramouni N, Ahmad MN, Zeaiter J. Analytical review of the catalytic cracking of methane. Fuel 2022;324:124455. https://doi.org/10.1016/j.fuel.2023.130427.
[18] Mokheimer EMA, Shakeel MR, Harale A, Paglieri S, Ben MR. Fuel reforming processes for hydrogen production. Fuel 2024;359:130427. https://doi.org/10.1016/j.fuel.2023.130427.
[19] Ping JN, Fairlie DM. X.-The methane equilibrium. J Chem Soc 1912;101:91–103.
[20] Ashik UPM, Wan Daud WMA, Abbas HF. Production of greenhouse gas free hydrogen by thermocatalytic decomposition of methane – A review. Renew Sustain Energy Rev 2015;44:221–56. https://doi.org/10.1016/j.rser.2014.12.025.
[21] Zhang J, Li X, Chen H, Qi M, Zhang G, Hu H, et al. Hydrogen production by catalytic methane decomposition: Carbon materials as catalysts or catalyst supports. Int J Hydrogen Energy 2017;42:19755–75. https://doi.org/10.1016/j.ijhydene.2017.06.197.
[22] Zavarukhin SG, Kuvshinov GG. Mathematic modeling of the process of production of nanofibrous carbon from methane in an isothermal reactor with a fixed bed of the $Ni-Al_2O_3$ catalyst. Chem Eng J 2006;120:139–47. https://doi.org/10.1016/j.cej.2006.03.004.
[23] Ammendola P, Chirone R, Ruoppolo G, Russo G, Solimene R. Some issues in modelling methane catalytic decomposition in fluidized bed reactors. Int J Hydrogen Energy 2008;33:2679–94. https://doi.org/10.1016/j.ijhydene.2008.03.033.
[24] Patzschke CF, Parkinson B, Willis JJ, Nandi P, Love AM, Raman S, et al. Co-Mn catalysts for H_2 production via methane pyrolysis in molten salts. Chem Eng J 2021;414:128730. https://doi.org/10.1016/j.cej.2021.128730.
[25] Upham DC, Agarwal V, Khechfe A, Snodgrass ZR, Gordon MJ, Metiu H, et al. Catalytic molten metals for the direct conversion of methane to hydrogen and separable carbon. Science 2017;358:917–21. https://doi.org/10.1126/science.aao5023.
[26] Hazer Group n.d. https://hazergroup.com.au/ (accessed June 21, 2023).
[27] BASF. Report 2021 - Methane pyrolysis n.d. https://report.basf.com/2021/en/shareholders/basf-on-the-capital-market/methane-pyrolysis.html (accessed June 21, 2023).
[28] Ammendola P, Chirone R, Ruoppolo G, Russo G. Production of hydrogen from thermo-catalytic decomposition of methane in a fluidized bed reactor. Chem Eng J 2009;154:287–94. https://doi.org/10.1016/j.cej.2009.03.048.
[29] Noh YG, Lee YJ, Kim J, Kim YK, Ha JS, Kalanur SS, et al. Enhanced efficiency in CO2-free hydrogen production from methane in a molten liquid alloy bubble column reactor with zirconia beads. Chem Eng J 2021;428:131095. https://doi.org/10.1016/j.cej.2021.131095.
[30] Kresse G, Hafner J. Ab initio molecular dynamics for liquid metals. Phys Rev B 1993;47:558–61. https://doi.org/10.1103/PhysRevB.47.558.
[31] Kresse G, Furthmüller J. Efficiency of ab-initio total energy calculations for metals and semiconductors using a plane-wave basis set. Comput Mater Sci 1996;6:15–50. https://doi.org/10.1016/0927-0256(96)00008-0.
[32] Kresse G, Furthmüller J. Efficient iterative schemes for ab initio total-energy calculations using a plane-wave basis set. Phys Rev B 1996;54:11169–86. https://doi.org/10.1103/PhysRevB.54.11169.
[33] Perdew JP, Burke K, Wang Y. Generalized gradient approximation for the exchange-correlation hole of a many-electron system. Phys Rev B 1996;54:16533–9. https://doi.org/10.1103/PhysRevB.54.16533.
[34] Arevalo RL, Aspera SM, Escaño MCS, Nakanishi H, Kasai H. Tuning methane decomposition on stepped Ni surface: The role of subsurface atoms in catalyst design. Sci Rep 2017;7:13963. https://doi.org/10.1038/s41598-017-14050-3.
[35] Gili A, Schlicker L, Bekheet MF, Görke O, Kober D, Simon U, et al. Revealing the mechanism of multiwalled carbon nanotube growth on supported nickel nanoparticles by in situ synchrotron X-ray diffraction, density functional theory, and molecular dynamics simulations. ACS Catal. 2019;9:6999–7011. https://doi.org/10.1021/acscatal.9b00733.
[36] Cabrera AL, Garrido MWH, Volkmann UG. Studies of carbon monoxide and hydrogen adsorption on nickel and cobalt foils aimed at gaining a better insight into the mechanism of hydrocarbon formation. Catal. Lett. 1994;25:115–26. https://doi.org/10.1007/BF00815421.
[37] Shin Y-H, Hong S. Carbon diffusion around the edge region of nickel nanoparticles. Appl. Phys. Lett. 2008;92:043103. https://doi.org/10.1063/1.2836265.
[38] Li Y, Li D, Wang G. Methane decomposition to COx-free hydrogen and nano-carbon material on group 8–10 base metal catalysts: A review. Catal. Today 2011;162:1–48. https://doi.org/10.1016/j.cattod.2010.12.042.
[39] Varvoutis G, Lykaki M, Stefa S, Binas V, Marnellos GE, Konsolakis M. Deciphering the role of Ni particle size and nickel-ceria interfacial perimeter in the low-temperature CO_2 methanation reaction over remarkably active Ni/CeO_2 nanorods. Appl. Catal. B Environ. 2021;297:120401. https://doi.org/10.1016/j.apcatb.2021.120401.
[40] Soliman AMS, Tschentscher R, Akporiaye D, Al-Rawashdeh M. Effect of Ni/SiO_2 catalyst preparation method on methane decomposition and CO_2 gasification cycles. Fuel 2024;368:131585. https://doi.org/10.1016/j.fuel.2024.131585.
[41] Tran R, Xu Z, Radhakrishnan B, Winston D, Sun W, Persson KA, et al. Surface energies of elemental crystals. Sci. Data 2016;3:160080. https://doi.org/10.1038/sdata.2016.80.
[42] Zheng H, Li X-G, Tran R, Chen C, Horton M, Winston D, et al. Grain boundary properties of elemental metals. Acta Mater. 2020;186:40–9. https://doi.org/10.1016/j.actamat.2019.12.030.
[43] Dupraz M, Li N, Carnis J, Wu L, Labat S, Chatelier C, et al. Imaging the facet surface strain state of supported multi-faceted Pt nanoparticles during reaction. Nat. Commun. 2022:13. https://doi.org/10.1038/s41467-022-30592-1.